

Nanoscale

Accepted Manuscript



This is an *Accepted Manuscript*, which has been through the Royal Society of Chemistry peer review process and has been accepted for publication.

Accepted Manuscripts are published online shortly after acceptance, before technical editing, formatting and proof reading. Using this free service, authors can make their results available to the community, in citable form, before we publish the edited article. We will replace this *Accepted Manuscript* with the edited and formatted *Advance Article* as soon as it is available.

You can find more information about *Accepted Manuscripts* in the [Information for Authors](#).

Please note that technical editing may introduce minor changes to the text and/or graphics, which may alter content. The journal's standard [Terms & Conditions](#) and the [Ethical guidelines](#) still apply. In no event shall the Royal Society of Chemistry be held responsible for any errors or omissions in this *Accepted Manuscript* or any consequences arising from the use of any information it contains.

ARTICLE

High quality large area MoSe₂ and MoSe₂/Bi₂Se₃ heterostructures on AlN(0001)/Si(111) substrates by molecular beam epitaxy

E. Xenogiannopoulou,^a P. Tsipas,^a K. E. Aretouli,^a D. Tsoutsou,^a S. A. Giamini,^a C. Bazioti,^b G. P. Dimitrakopoulos,^b Ph. Komninou,^b S. Brems,^c C. Huyghebaert,^c I. P. Radu,^c and A. Dimoulas^{*a}

Cite this: DOI: 10.1039/x0xx00000x

Received 00th January 2012,
Accepted 00th January 2012

DOI: 10.1039/x0xx00000x

www.rsc.org/

Atomically thin inherently 2D semiconductors offer thickness scaling of nanoelectronic devices and excellent response to light for low power versatile applications. Using small exfoliated flakes, advanced devices and integrated circuits have already been realized showing their great potential to impact nanoelectronics. Here, high quality single crystal MoSe₂ is grown by molecular beam epitaxy on AlN(0001)/Si(111) showing the potential for scaling up growth to low cost, large area substrates for mass production. The MoSe₂ layers are epitaxially aligned with the aluminum nitride (AlN) lattice showing uniform, smooth surface and interfaces with no reaction or intermixing and with sufficiently high band offsets. High quality single layer MoSe₂ are obtained with a direct gap evidenced by angle resolved photoemission spectroscopy and further confirmed by Raman and intense room temperature photoluminescence. Successful growth of high quality MoSe₂/Bi₂Se₃ multilayers on AlN shows promise for novel devices exploiting the non-trivial topological properties of Bi₂Se₃.

Introduction

The isolation of various 2D layered transition-metal dichalcogenides (TMDs) in recent years, gave a large boost in the research for designing Van der Waals 2D structures with tailored properties depending on the material and the layer thickness.¹⁻³ TMDs with the general chemical formula MX₂ (M=Mo, W; X= S, Se, Te) are indirect semiconductors exhibiting an indirect to direct band gap crossover when thickness reduces from few layers to a single layer. The direct band gap in single layers results in intense room temperature photoluminescence (PL)⁴ and more generally yields excellent response to light in the visible and near IR region of the solar spectrum, enabling a wide range of applications from optoelectronics⁵⁻⁸ to energy conversion.⁸ Owing to their strong covalent bonds within the MX₂ molecule, these materials exhibit high mechanical strength and since they can be grown few atom-thick, they are stretchable and bendable so they could be used for flexible transparent displays and a number of low power versatile applications.¹ Besides, the low dielectric constant (~4) and the ability to reduce the channel to a single layer of atoms without severely degrading mobility offer excellent electrostatic control allowing for aggressive lateral scaling beyond that presently achieved using silicon or other conventional semiconductors.

Using TMDs, mainly MoS₂, advanced field effect transistors⁹⁻¹¹ and generic integrated circuits (e.g. inverters, ring oscillators, SRAM, NOR gates)^{12,13} have been demonstrated, showing this material's potential to impact nanoelectronics. So far, most of the research device work⁹⁻¹² has been performed on small (micron-sized) exfoliated flakes, while for mass production, large area synthesis of TMDs on insulating substrates is required to ensure reproducibility, high crystalline quality and homogeneity and ease of device fabrication. Most attempts to synthesize TMDs are based on CVD-like methods used first for the growth of MoS₂¹⁴ and then applied to MoSe₂ growth.¹⁵⁻¹⁷ These methods produce single crystals with sizes up to a few hundred microns,¹⁶ however, polycrystallinity, incomplete coverage and thickness uniformity are important issues.

Molecular Beam Epitaxy (MBE) of MoSe₂ on suitable crystalline substrates is expected to give highly oriented single crystals over the entire wafer. Apart from early pioneering work¹⁸ there is a very recent report on the MBE growth of atomically thin epitaxial MoSe₂ on graphene-terminated 6H-SiC (0001) substrates¹⁹ mainly focusing on the electronic band structure by angle resolved photoelectron spectroscopy (ARPES). There is little information about the structural quality, the band alignment and the optical emission properties

of epitaxial single and few-layer MoSe₂ grown by MBE on alternative insulating substrates.

In this work, we demonstrate high quality few layer (1-6 ML) MoSe₂ which are grown epitaxially on AlN(0001)/Si(111) substrates by MBE with or without a buffer layer. We show that using AlN crystalline templates it is possible to obtain highly oriented single crystals of single- or few- layer MoSe₂ over the entire wafer (up to two inches) exhibiting high quality, very good uniformity and excellent stability in air, as verified by Raman characterization and room temperature photoluminescence. We also show that very good quality MoSe₂ can be grown on Bi₂Se₃ and that epitaxial Bi₂Se₃/MoSe₂ multilayers can be produced, thus creating the prospect for novel devices to exploit the non-trivial topological insulator properties²⁰ of Bi₂Se₃.

Experimental

Thin film growth and structural characterization

Films growth is carried out in an UHV-MBE system with base pressure in the 10⁻¹⁰ Torr range. All growth procedures are monitored by Reflection High Energy Electron Diffraction (RHEED) technique using a 15 keV e-gun. MoSe₂ is deposited either directly on 200nm AlN/Si(111) substrates or with a thin (3 or 5 quintuples (QL)) epitaxial Bi₂Se₃ buffer layer.

The 200 nm Al-face AlN(0001) layers are epitaxially grown by MOCVD on B-doped p-type 1150 μm Si(111) substrates, with a resistivity > 1 Ohm-cm. AlN is unintentionally n-type doped, typical for MOCVD grown AlN layers. The AlN substrates received both *ex situ* and *in situ* cleaning in the MBE chamber, following the procedure described in Ref. 20.

High purity Mo (99.95%) and Se (99.999%) are evaporated from an electron-gun evaporator and an effusion cell respectively, under Se-rich conditions with Mo/Se flux ratio of ~1:10 and a MoSe₂ growth rate of 3 ML/min. Bi₂Se₃ buffer layer growth on 200nm AlN(0001)/Si(111) substrate is performed by evaporating Bi(99.997%) and Se (99.999%) both from effusion cells with a Bi/Se flux ratio of ~1:20 and a growth rate of 1.5QL/min.

After MoSe₂/AlN layers deposition, samples are transferred in the STM chamber attached to the MBE growth chamber for *in situ* STM characterization. STM topographies were obtained in UHV (base pressure of low 10⁻⁹ mbar) at RT using an Omicron Large Sample SPM microscope with a Pt/Ir tip.

For the HRTEM characterization, cross-section TEM specimens are prepared by the sandwich technique. Mechanical grinding followed by focused Ar⁺ ion milling in the GATAN PIPS is used to thin the specimens to electron transparency. HRTEM observations are performed using a 200 kV JEOL 2011 microscope, spherical aberration coefficient Cs=0.5 mm and point resolution 0.192 nm. Thickness-defocus HRTEM image maps are simulated using the EMS²¹ software package and are associated to the HRTEM experimental images.

Physical and chemical characterization

In situ ARPES is conducted at RT in a μ-metal analytical chamber equipped with a 100 mm hemispherical electron analyzer (SPECS PHOIBOS100) and a 2D CCD detector. The energy resolution of the detection system is better than 40meV, while the total experimental energy resolution is ~ 100meV^{22,23} dominated by the thermal broadening at RT. The excitation source is a He discharge lamp (SPECS UVS35/10) with He I (He II) radiation at 21.22 eV (40.814 eV). Photoelectrons

emitted by the samples are measured in the energy distribution curve (EDC) mode. *In situ* x-ray photoelectron spectroscopy (XPS) is performed with excitation by Mg-K_α radiation (1253.6 eV) using a SPECS XR50 source, at take-off angle of 52°.

For Raman spectroscopy a 532 nm laser beam is used with a power of ~2mW on the sample surface. Spectra are resolved by a spectrometer using a grating of 1800 l/mm and acquired by an EMCCD detector. A 100x objective lens is used and the FWHM of the laser beam intensity at the sample surface is ~1 μm. For the photoluminescence (PL) spectroscopy measurements, a 100x objective lens is used in combination with a grating of 600 l/mm. Both Raman and PL measurements are performed at RT.

Electronic structure calculations

The calculations are performed within the density functional theory (DFT) framework by using the Vienna ab initio simulation package. The Perdew-Burke-Ernzerhof with dispersion (PBE-D) exchange-correlation functional is engaged for our calculations. Spin-orbit effects are treated self-consistently. All atoms are allowed to relax until the force and the energy is converged to 10⁻² eV/Å and 10⁻⁴ eV, respectively.

Results and discussion

MoSe₂ growth on AlN and on Bi₂Se₃ buffer layer

MoSe₂ is grown using a two-step process. Initially, MoSe₂ is deposited on AlN/Si(111) substrates at the relative low temperature of 350 °C, where a blurred RHEED pattern is observed indicating poor crystalline quality. In the second step, a post-deposition annealing in UHV is performed at 690 °C. The result is that the crystallinity is substantially improved as evidenced by the RHEED streaky pattern in (Figs. 1g, h) although a slightly disordered surface may not be excluded considering that the streaks are not as sharp as in the case of clean AlN surface (Fig. 1a, b). The streaky RHEED pattern in both [11-20] and [1-100] azimuths of a 1ML MoSe₂ in Figs. 1g and 1h respectively, indicates that the two hexagonal unit cells are perfectly aligned such that [11-20]_{MoSe2}//[11-20]_{AlN} and [1-100]_{MoSe2}//[1-100]_{AlN} in the plane. It is worth noting that the RHEED beam covers an area of a few mm at least, which is a significant portion of the cm-scale wafer. The absence of additional streaks indicates also the absence of rotated 30 or 90 deg domains meaning that the layers are highly oriented single crystals extended over large part, if not the entire wafer. The small, almost undetectable difference in the relative positions of the streaks (Fig. 1a, g) reflects the rather small lattice mismatch of ~ 6% between the MoSe₂ and AlN (a_{AlN} = 3.11Å, a_{MoSe2} = 3.299Å) at room temperature; the latter nearly matched condition may be the reason for the perfect orientation of MoSe₂ crystal relative to the substrate.

Recently, our group reported²⁰ the high quality epitaxial growth of Bi₂Se₃ thin films on AlN(0001) substrates, which motivated us to use 5 quintuple layers (QL) of Bi₂Se₃ as a buffer layer for 2ML MoSe₂ overgrowth. The results in Fig. 1i-n show that both Bi₂Se₃ and MoSe₂ layers are epitaxial and perfectly oriented with the AlN substrate such that [11-20]_{MoSe2}//[11-20]_{Bi2Se3}//[11-20]_{AlN} and [1-100]_{MoSe2}//[1-100]_{Bi2Se3}//[1-100]_{AlN}. It is remarkable that MoSe₂ is grown highly oriented on Bi₂Se₃ despite the large mismatch of about 20% between the two materials. The growth of MoSe₂ is constrained to low temperatures due to the limited thermal stability of the underlying Bi₂Se₃ buffer which decomposes in vacuum at

temperatures higher than 300 °C. Nevertheless, the presence of the Bi₂Se₃ buffer layer promotes the growth of MoSe₂ at much lower substrate temperatures (300 °C) compared to the direct deposition on AlN(0001) substrate (690 °C) without reduction in epitaxial quality. The ability to lower the growth temperature of such 2D materials could be advantageous for large scale device manufacturing especially for applications where heterogeneous integration with Si devices is required.

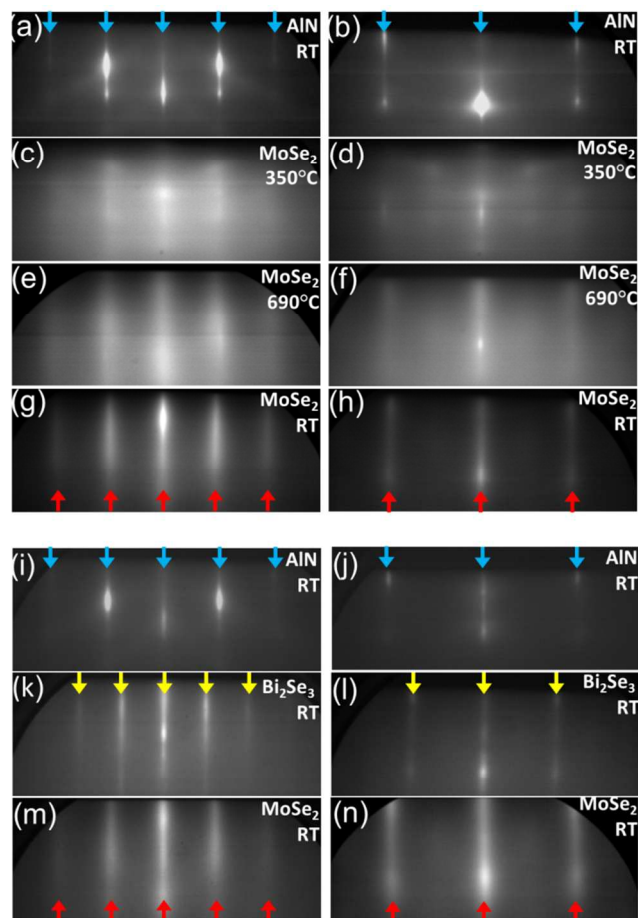


Fig. 1 RHEED patterns of: (a-h) 1ML MoSe₂ deposited on AlN(0001) with the 2 step-process and (i-n) 2ML MoSe₂ deposited on 5QL Bi₂Se₃ buffer layer epitaxial grown on AlN(0001). (a, i) show bare AlN(0001) pattern along [11-20] azimuth and (b, j) bare AlN(0001) along [1-100] azimuth. (c, d) are recordings at 350 °C after the deposition of MoSe₂, (e, f) are recordings at 690 °C, after the post-deposition annealing step while (g, h) present the MoSe₂ film on AlN after final cooling down to RT. (e, f) MoSe₂ becomes high crystalline with the respective crystal orientations aligned to those of AlN which is clearly observed after cooling down in (g, h). (k, l) 5QL Bi₂Se₃ buffer layer grows epitaxial on AlN(0001) at 300 °C with high crystalline quality, (m, n) MoSe₂ deposited on Bi₂Se₃ buffer layer at 300 °C grows epitaxial with [11-20]_{MoSe₂}//[11-20]_{Bi₂Se₃} and [1-100]_{MoSe₂}//[1-100]_{Bi₂Se₃}. Blue and yellow downward arrows show AlN and Bi₂Se₃ streaks respectively. Red upward arrows show MoSe₂ streaks.

Film structural characterization

The surface structure of a 3 ML MoSe₂ sample is imaged *in situ* by UHV-STM as depicted in Fig. 2. The high resolution image (Fig. 2a) shows the hexagonal symmetry of the lattice. The

brighter spots in Fig. 2a represent Se atoms located in the three corners of the top hexagon (Fig. 2b)²⁴ separated by a distance of 3.3 Å as shown in the line scan 1 of Fig 2c. This is in good agreement with the theoretical value of the lattice constant a_{MoSe_2} =3.299 Å. The Mo atoms are located in the three corners of the hexagon located 1.67 Å below the top one (see also ESI†, Fig. S1a). This picture is further supported by the line scan 2 in Fig. 2d showing that Mo atoms are in a lower position and have a distance of ~ 2 Å from neighboring Se atoms, close to the theoretical value of 1.9 Å. STM performed in a larger scale (see ESI†, Fig. S2a, b), reveals that at the low deposition temperature the sample has root-mean-square (RMS) surface roughness value of 1.25 nm which however significantly improves after post-deposition annealing (see ESI†, Fig. S2c, d) yielding an RMS roughness of 0.62 nm, over a scanned areas of (5x5) μm². The annealed sample shows a continuous film with smooth surface morphology.

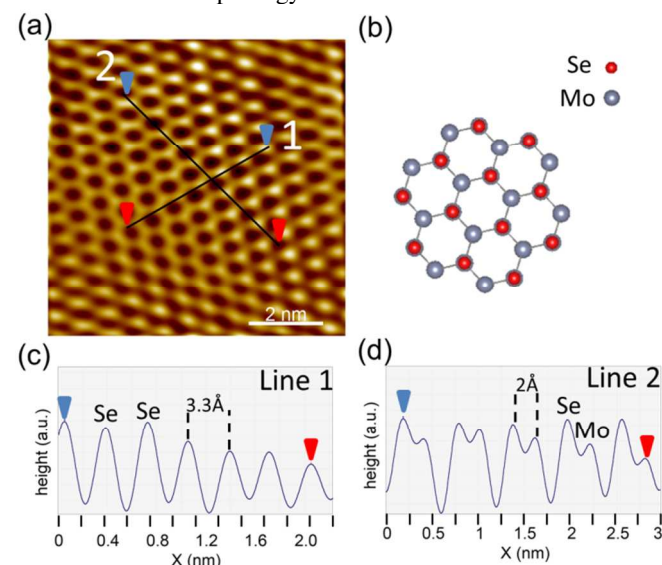


Fig. 2 (a) Room temperature high resolution STM image of 3ML MoSe₂ on AlN(0001) (Ubias=0.7 V, I= 0.9 nA) showing a honeycomb structure. The brighter corners in the honeycomb configuration are attributed to Se atoms occupying the three corners of the topmost hexagon. (b) Stick and ball model of MoSe₂ honeycomb structure along the [0001]_{MoSe₂} axis showing the Se and Mo atoms positions. Se atoms reside on the three corners of the top hexagon while Mo occupies the three corners of a hexagon located 1.67 Å from the top one. (c) Profile along line 1 in image (a) showing the estimated distance of 3.3 Å between Se-Se atoms, in good agreement with the MoSe₂ lattice constant a_{MoSe_2} =3.299 Å. (d) Profile along line 2 in image (a) showing the buckling between Se-Mo atoms and their estimated lateral distance of 2 Å, close to the theoretical value of 1.9 Å.

Additionally large area optical images of samples with different size and parts of a sample inspected by SEM, (see ESI†, Fig. S3) indicate a uniform, homogeneous film over the entire substrate.

The films microstructure is examined by High Resolution Transmission Electron Microscopy (HRTEM) (Fig. 3). A low magnification cross section TEM image is presented in Fig. 3a, showing a 3 ML MoSe₂ film of uniform thickness and smooth surface and interface with AlN substrate, as also verified by large area STM images (see also ESI†, Fig. S2).

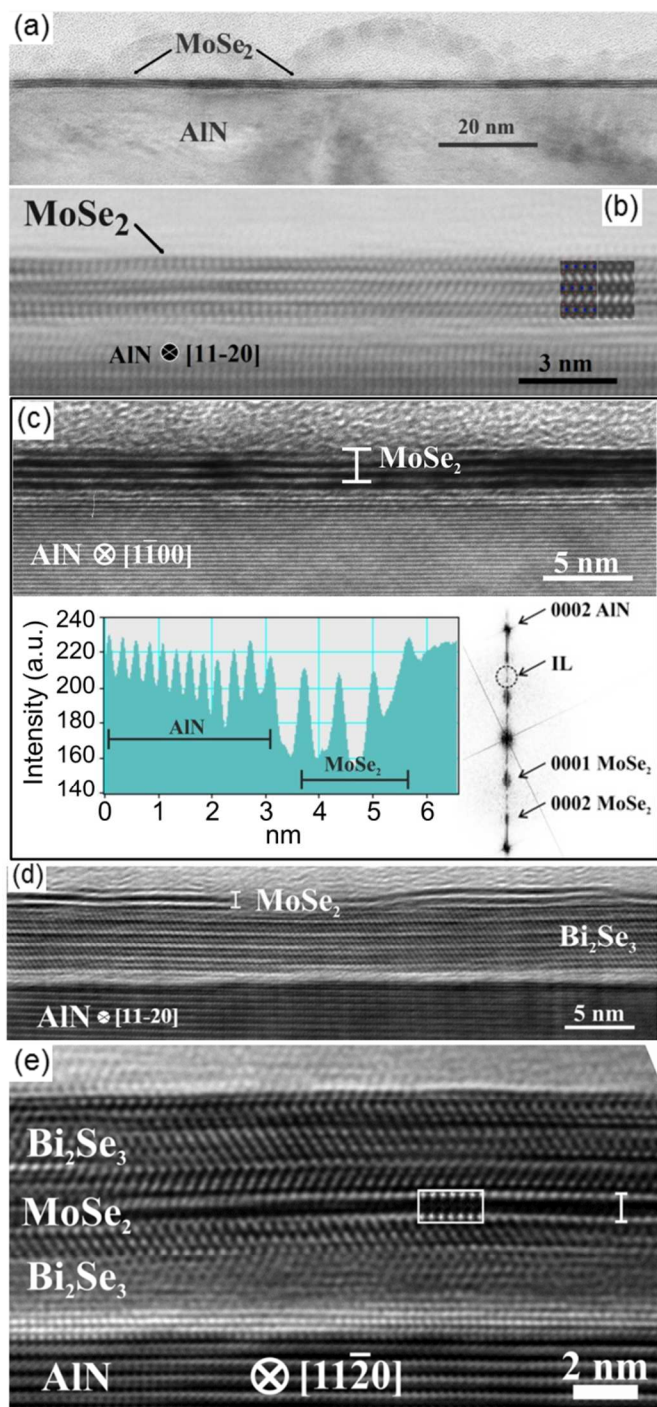


Fig. 3 (a-c) Cross-section HRTEM images of 3 ML MoSe₂ grown on AlN(0001) viewed in low magnification (a), along the [11-20]_{AlN} with the corresponding simulated image as inset in (b) and along the [1-100]_{AlN} in (c). In (b) and (c), MoSe₂ is located in the darker contrast areas, while the very bright rows, more pronounced in (c), show the separation between the MoSe₂ layers. In (c) a crystalline MoSe₂/AlN interface is shown with the corresponding absorption contrast profile (left side) presenting lattice fringes. The fringe spacing at the top three AlN layers increases gradually. The Fast Fourier Transform (FFT) (right side) calculated from the HRTEM image is presented showing the points that represent the spatial frequencies contained. (d) HRTEM images of 2ML MoSe₂

deposited on 5QL Bi₂Se₃ buffer layer grown on AlN(0001) viewed along [11-20]_{AlN}. (e) 3QL Bi₂Se₃/2ML MoSe₂/3QL Bi₂Se₃ heterostructure deposited on AlN(0001) at 300 °C viewed along [11-20]_{AlN} (inset the corresponding MoSe₂ simulated image). (b-e) show that MoSe₂ grows epitaxially with high crystalline quality on both AlN and Bi₂Se₃ buffer layer on AlN. The MoSe₂ films grown on AlN show a smooth surface and interface morphology.

The HRTEM image of Fig. 3b shows 3 layers of MoSe₂ imaged along the [11-20]_{AlN} zone axis. The corresponding simulated image (thickness 15 nm along the electron beam, defocus -70 nm) superimposed on the right side confirms that the [11-20] directions of AlN and MoSe₂ lattices are aligned in agreement with the RHEED data in Fig. 1. The intense bright rows correspond to space between MoSe₂ layers (Se atoms appear dark) whilst Mo atoms relate to the bright dotted rows in between (see also ESI†, Fig. S1b). Fig. 3c shows the same sample imaged along the [1-100]_{AlN} zone axis. Similarly, dark rows correspond to the MoSe₂ layers and bright areas to the space between them. Because of the dense atom configuration along this direction (see also ESI†, Fig. S1c), no atoms are resolved in the dark areas in contrast to Fig. 3b. Figs. 3d and 3e show 2 ML of MoSe₂ grown on top of 5QL epitaxial Bi₂Se₃ buffer and 2ML of MoSe₂ sandwiched between two Bi₂Se₃ layers, 3QL-thick each, respectively. The corresponding image simulation is shown as inset in Fig. 3e (thickness 8.5 nm, defocus -70 nm) in which bright dotted rows correspond to Mo atoms. In summary, the data in Fig. 3 (combined with the RHEED data) show that high quality epitaxial MoSe₂ and MoSe₂/Bi₂Se₃ multilayers can be grown on AlN substrates with flat surface morphology and clean, crystalline interfaces.

A small distortion of AlN just underneath MoSe₂ can be seen in Figs. 3b and 3c. The appearance of an interlayer in the TEM pictures in a first approach could be attributed to an artifact. Ion milling certainly affects this interface preferentially, given the weakness of the van der Waals bonding and the fact that AlN is easily amorphized under the ion beam. In this regard, some interfacial damage is expected during sample preparation. The brighter contrast of the AlN lattice fringes at the interface could be attributed to the locally smaller thickness of the foil due to the preferential thinning mentioned above. Therefore, the interfacial region is not amorphous in the as-grown sample and any amorphization is induced by the ion milling during TEM specimen preparation.

In a closer examination of the interface, we have undertaken detailed measurements of lattice fringe spacings from cross sectional HRTEM images²⁵ in Fig. 3c. Our measurements, supported by the absorption contrast profile, showed a gradual increase of the (0002) *d*-spacing between the top 3 or 4 AlN lattice fringes as shown in Fig. 3c. Furthermore, a strain mapping performed using geometrical phase analysis (GPA)²⁶ (see also ESI†, Fig. S4), showed an increase of up to 20% in the spacing of these fringes. The local increase of the lattice constant could be attributed either to a change in chemical composition, or to elastic strain, or to both. Elastic strain, if present, could even promote the local amorphization of these top layers under ion beam milling. A possible cause for the increase of the *d*-spacing is the modification of the top 3-4 AlN layers through the incorporation of molybdenum atoms. Mo has a higher electron affinity than Al, and a larger atomic radius. The absorption contrast profile in Fig. 3c shows an increase of the lattice parameter by up to ~20% prior to the MoSe₂ film. Hexagonal molybdenum nitride has a 13% larger lattice constant than AlN

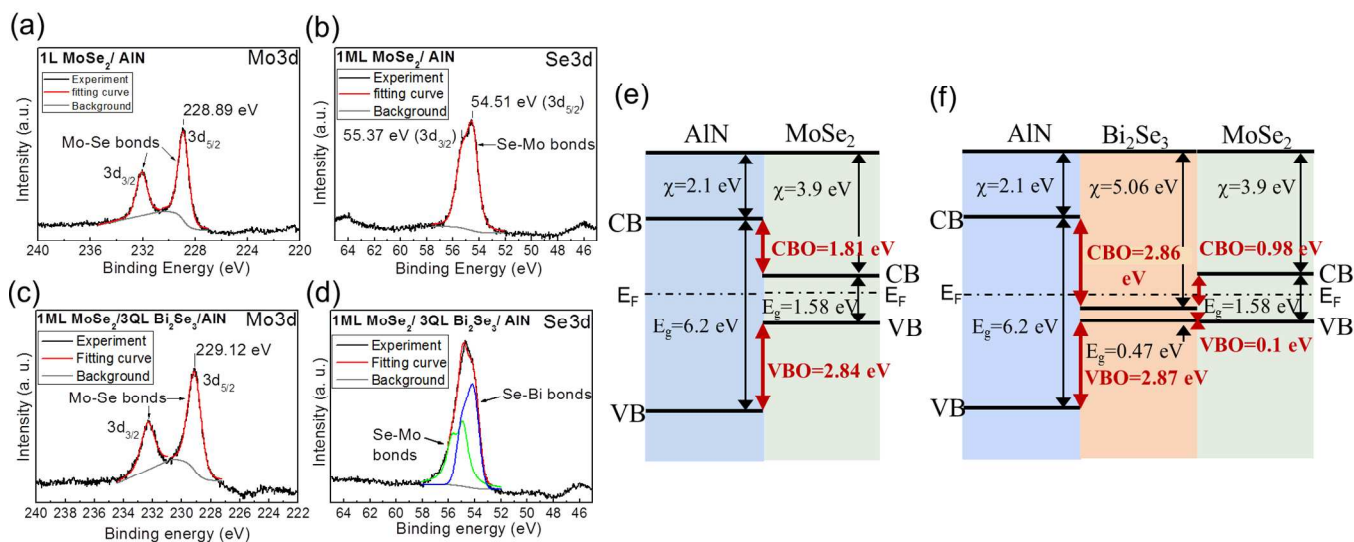


Fig. 4. (a, b) Mo3d, Se3d core level XPS peaks of 1ML MoSe₂ grown on AIN. No reaction with the substrate is observed and the positions and lineshape of Mo3d and Se3d peaks indicate Mo-Se bonding. (c, d) Mo3d, Se3d, core level XPS peaks of 1ML MoSe₂ deposited on 3QL Bi₂Se₃ buffer layer on AIN. The Se3d peak is attributed to Se-Mo and Se-Bi bonding while Mo3d peaks indicate Mo-Se bonding. (e, f) Schematic of the MoSe₂/AIN and MoSe₂/Bi₂Se₃/AIN band offsets, as determined by XPS core level analysis. χ and E_F denote the electron affinity and the Fermi energy, respectively. E_g is the energy gap while CBO and VBO denote the conduction and valence band offsets, respectively.

along the growth direction,²⁷ so we anticipate that some elastic strain is also present. The possible reaction between MoSe₂ and AIN at the interface is further studied by X-ray Photoelectron Spectroscopy (XPS) below.

Interface and band alignment characterization by XPS

In situ X-ray photoelectron Spectroscopy is applied to both MoSe₂/AIN and MoSe₂/Bi₂Se₃/AIN heterostructures. The binding energies of Mo3d_{5/2} and Se3d_{5/2} core levels for 1ML MoSe₂ deposited directly on AIN(0001) (Fig. 4a, b) are 228.89 eV and 54.51 eV respectively. These values are in good agreement with other reported¹⁸ on thin film and bulk single crystal MoSe₂. The core level peaks positions and lineshapes indicate that only Mo-Se bonds exist. Therefore, within the detection limit of our XPS it can be inferred that MoSe₂ does not react with the AIN substrate in large quantities. A limited incorporation of Mo in the top 3 layers of AIN may not be excluded though taking into consideration the HRTEM analysis of the image in Fig. 3c as described in the previous section. Similarly, in the case of 1ML MoSe₂ deposited on 3QL Bi₂Se₃ buffer layer on AIN at 300 °C (Fig. 4c, d) the Mo3d_{5/2} peak position at 229.12 eV indicates Mo-Se bonds and agrees well with MoSe₂ formation while the Se3d peak is attributed to two contributions, one to Se-Mo bonds and one to Se-Bi bonds. The Bi4f_{7/2} core level binding energy of 158.52 eV (not shown here), indicates that Bi is bonded only with Se and no reaction at Bi₂Se₃/AIN interface occurs. In addition, using tabulated sensitivity factors the Se/Mo ratios are found to be in the range of (1.9-2.05) indicating that the layers have stoichiometry close to the ideal one that is Se/Mo=2/1.

The band offsets of the MoSe₂/AIN and MoSe₂/Bi₂Se₃/AIN heterojunctions were derived from XPS measurements (Fig. 4e, f). In particular, the valence band offsets (VBO) have been determined using Kraut's method²⁸ to be 2.84 eV and 2.87 eV/0.1 eV for the MoSe₂/AIN and Bi₂Se₃/AIN systems,

respectively (see also ESI†). Accordingly, the conduction band offsets (CBO) have been calculated to be 1.81 eV and 2.86 eV/0.98 eV for the MoSe₂/AIN and Bi₂Se₃/AIN systems, respectively, using band gap values (see also ESI†) taken from the literature. The estimated CBO and VBO between the MoSe₂ and AIN indicate sufficiently high transport barrier for both electrons and holes perpendicular to the layers, implying that the AIN layer could provide sufficient insulation for the operation of MoSe₂-based electronic devices with minimum leakage through the substrate. It is worth noting that the XPS reconstructed band alignments are consistent with electron affinity values (see Fig. 4e, f) reported in the literature for AIN, MoSe₂ and Bi₂Se₃ materials²⁹⁻³¹ and the position of the Fermi level E_F with respect to the CB and VB of the layers in the stack, suggesting that there is no band bending or charge transfer at the interfaces.

Electronic band structure of MoSe₂ films

Fig. 5 shows the valence band structure of 1 to 6 ML MoSe₂ films grown on AIN(0001) substrates as imaged by ARPES in the Γ KHA plane of the 1st BZ of MoSe₂^{22,32} using He I (21.22 eV) and He II (40.814 eV) excitation energies. Except for the spin-splitting of the band near K which is not resolved because of limited resolution (~110 meV) at room temperature, in the monolayer limit, the observed band dispersion along Γ -K (Fig. 5a, d) agrees quite well with the theoretical calculations (Fig. 5g). The VB maximum is located at the K-point with a binding energy $E_B=1$ eV, about (150-200) meV higher in energy than at the Γ point. Comparison with first principles calculations (Fig. 5g), which predict a conduction band minimum also at the K point, indicates that our nominal single layer MoSe₂ films have a direct band gap.^{19,33,34} As thickness increases to 3ML (Fig. 5b, e) and 6 ML (Fig. 5c, f) the VB maximum switches to the Γ/A -point, due to a shift of the topmost valence band to lower binding energies (closer to E_F) around Γ/A -point, while its

position at K/H-point remains at the same level. Thus, in thicker films the VB maximum is located at the Γ /A-point (Fig. 5e, f) resulting in an indirect band gap as predicted³³ in bulk TMDs or observed¹⁹ in 8-ML-thick MoSe₂ films. The thickness dependence of the VB maximum around Γ /A-point is clearer in the He II data (Fig. 5 d-f).

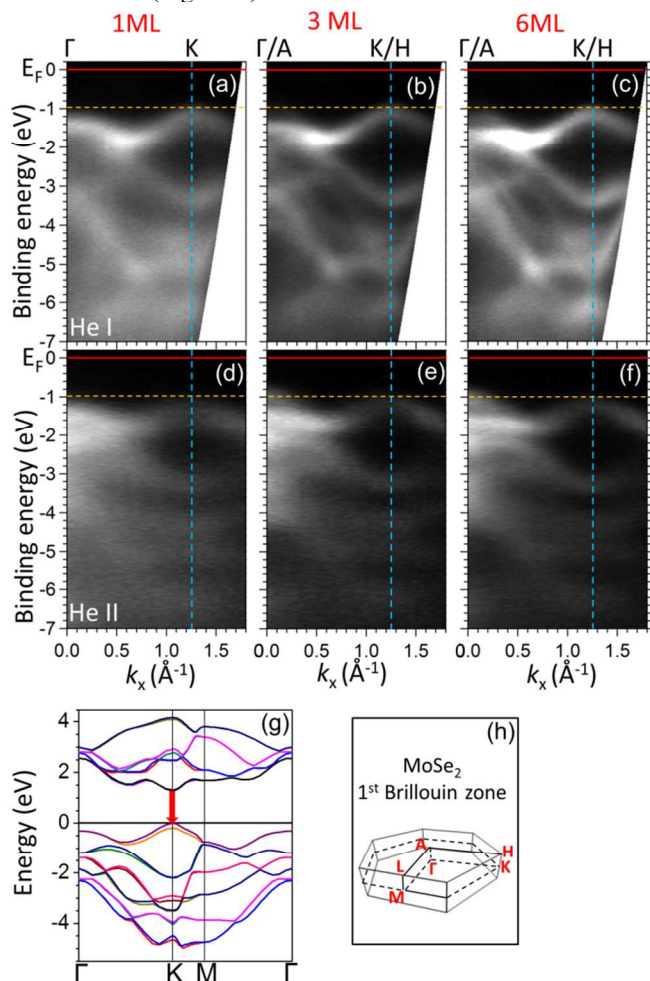


Fig. 5 Valence band structure imaging by ARPES of (1 to 6ML) MoSe₂ layers grown on AlN(0001) substrates along the Γ /A-K/H direction of the 1st BZ of MoSe₂. Measurements made at RT, using (a-c) He I (21.22 eV) and (d-f) He II (40.814 eV) resonance radiations. The images in (a-f) show the binding energy as a function of the wavevector component $k_{\parallel,x}$ parallel to the surface. In the monolayer limit (a, d) the VBM is located at the K-point at $E_B=1$ eV indicating a direct band gap. In thicker films, at 3ML (b, e) and 6ML (c, f) the VBM is located at the Γ -point which is consistent with an indirect band gap. Among He I and He II data at 3ML (b, e) and 6ML (c, f) films, small differences in the band structure around the Γ -point are observed. This is attributed to a small $E(\vec{k}_{\perp})$ dispersion around the Γ -point. Red solid lines indicate the E_F level position, while orange dashed lines indicate the position of VBM at K/A point. (g) First principle calculated band structure of 1ML. The red arrow indicate the direct band gap position, (h) the first Brillouin zone of 2H structure of MoSe₂.

The small difference between He I and He II data is due to a weak dispersion $E(\vec{k}_{\perp})$ around the zone center^{22,32} which is picked up by the different photon excitation energies. As thickness increases, mainly $Mo\ 4d_{z^2}$ orbitals^{22,23,32-34} contribute to the VBM around the Γ -point through the vdW-interlayer-interaction³³ showing its bulk character. On the other hand the topmost VB around K-point shows negligible thickness dependence due to the $Mo\ 4d_{xy/x^2-y^2}$ origin.^{22,23,32-34} The data

in Fig. 5 present well resolved spectra characteristic of energy dispersion along the Γ K crystallographic direction in k-space in agreement with theory. This supports our claim made on the basis of RHEED in Fig. 1 that the films are highly oriented essentially forming a single crystal. If several orientation domains existed, then a more complex and fuzzy dispersion would have been observed in Fig. 5, characteristic of a mixture of dispersions along different crystallographic orientations, which is not the case here.

Film quality and thickness uniformity by Raman and PL

The vibrational modes of the prepared monolayer MoSe₂ film on 200nm AlN(0001)/Si(111) is investigated by Raman spectroscopy. The group theory analysis for bulk TMDs which are members of D_{6h} point group symmetry,³⁵ predicts four Raman active and two Raman inactive modes. From the active modes only the in plane mode E_{2g}^1 and the out-of-plane mode

A_{1g} are accessible under the experimental conditions.

Additionally, one Raman mode that is inactive in bulk crystals, becomes optically active when the number of layers decreases due to the breakdown of translation symmetry.^{15,35} This is an interlayer vibrational mode B_{2g}^1 characterized as breathing mode and is present only in few-layer material and absent in a single layer MoSe₂.

The typical Raman spectrum of single layer MoSe₂ on AlN shown in Fig. 6a, has two intense sharp Raman peaks. One is attributed to the MoSe₂ out-of-plane vibrational mode A_{1g} at 240.8 cm⁻¹ and one to the crystalline Si³⁵ substrate at 521 cm⁻¹. The in-plane E_{2g}^1 mode of MoSe₂ is located at 288.5 cm⁻¹ (clearly shown in the expanded Raman spectrum in the region of (200-400) cm⁻¹ in Fig. 6d). There is no evidence of the breathing mode B_{2g} peak around 352 cm⁻¹, an area of the spectrum which is dominated by weak background signals. The bands centered at 303 cm⁻¹ and 960 cm⁻¹ (Fig. 6a) are associated with the 2TA and 2TO modes of crystalline Si.³⁶

From the peak positions of the Raman shifts and their intensities it is difficult to distinguish between monolayer and bilayer MoSe₂. However, most of the evidence in this work is in favor of monolayer MoSe₂ and it is in good agreement with published data of monolayer MoSe₂ either transferred^{35,37} or grown^{15,17,38} on SiO₂/Si substrates. The intensity ratio between out-of-plane A_{1g} and in plane E_{2g}^1 modes (A_{1g}/E_{2g}^1) is found to be ~ 23 , in agreement with published values for exfoliated single layer MoSe₂.^{37,39} In addition, the weak or totally absent breathing mode (Fig. 6d) points to single layer MoSe₂ material.

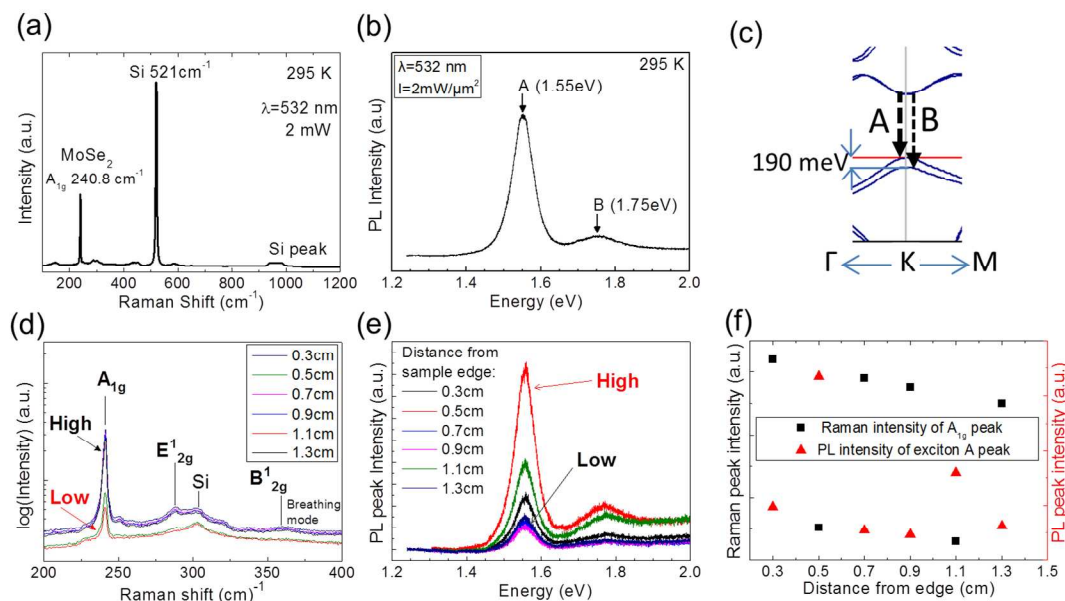


Fig. 6 (a-c) Characterization of nominally single layer MoSe₂ on AlN(0001) (a) Raman spectrum showing the A_{1g} peak at 240.8 cm⁻¹ associated with MoSe₂. (b) Photoluminescence spectrum showing the presence of two excitonic peaks at 1.55 eV and 1.75 eV (c) schematic detail of theoretical band structure around the K-point of 1 ML MoSe₂, indicating the two excitonic transitions A and B with 190meV energy difference due to spin-orbit splitting. The theoretically predicted energy difference is in good agreement with the measured PL peaks energy difference in (b). (d-f) Large scale uniformity investigation of (2x2) cm² sample of the same MoSe₂ sample on AlN(0001). (d) Raman spectra and (e) photoluminescence spectra measured at variable distances from sample edge. (f) Correlation of Raman and PL peaks intensities measured at variable distances from sample edge. On large scale area two different behaviors are observed. The high Raman signal of A_{1g} peak is correlated to the low PL intensity of exciton A and vice versa.

Photoluminescence spectroscopy was used to investigate optical emission properties of monolayer MoSe₂ grown on AlN with the main aim to probe the quality of the layer and verify that the material has a direct band gap as indicated by *in-situ* ARPES. The epitaxially-grown single-layer MoSe₂ on AlN presents strong PL emission at room temperature, as shown in Fig. 6b, with a dominant peak at 1.55 eV and a weaker peak at 1.75 eV, attributed to direct excitonic transitions A and B, respectively, corresponding to the transitions schematically shown in Fig. 6c. Due to loss of inversion symmetry in monolayer MoSe₂, the VB degeneracy is lifted^{19,40} under the influence of strong spin-orbit interaction resulting in the VB splitting near the K-point as predicted by DFT (Fig. 6c) and probed by PL (Fig. 6b). The measured energy difference of ~200meV between the two PL signals, agree very well with the calculated spin-orbit splitting of ~190 meV in Fig. 6c as well as with published experimental¹⁵ and theoretical values.⁴⁰ The strong PL signal in Fig. 6b indicates direct gap material in accordance with the nominally 1 ML thickness of the grown MoSe₂, although the possibility to obtain similar double peak PL at the same energy from a bilayer MoSe₂ cannot be excluded.

To extract information about uniformity in terms of structural and optical properties, the sample is probed over the entire 2 cm square substrates. At short scale, in an area of (40 x 40) μm², a highly uniform layer in terms of Raman A_{1g} peak intensity, width and position is revealed (see also ESI†, Fig. S5). In general, Raman

selection rule does not exclude a dependence of the Raman peak intensities on the crystal orientation which should reflect in the polarization of the scattered light. However, the Raman experimental set-up used here does not have an analyzer so the detection system lacks sensitivity with respect to the polarization of the scattered radiation from the sample. Therefore, the peak intensities do not depend on the crystal orientation as verified by arbitrarily rotating the sample (not shown here). Given the insensitivity of the different Raman peaks to crystal orientation, the intensity ratio between A_{1g} and E_{2g}¹ is an appropriate parameter for an accurate uniformity assessment of the MoSe₂ film. Since the E_{2g}¹ peak is small and overlaps with a nearby Si peak, both peaks are fitted simultaneously and the height of the E_{2g}¹ peak is extracted. An example of a E_{2g}¹ fitting result is given in Fig. S5. It is clear that the A_{1g} / E_{2g}¹ Raman mapping (see also ESI†, Fig. S5) indicates a uniform MoSe₂ layer over a 40 x 40 μm² area with an average value of A_{1g} / E_{2g}¹ ratio of ~ 23, indicative of monolayer MoSe₂.³⁷

On a larger scale, the sample is probed along a line which runs across the substrate from one edge to the other with 200 μm steps and the results are summarized in Figs 6d, e. Although the sample is very uniform over large areas, the data show a remarkable “digital” behavior mainly revealed in the Raman

spectra (Fig. 6d). The Raman A_{1g} mode acquires either low or high values but no values in between. The PL (Fig. 6e) follows a similar behavior although with a larger dispersion in intensity. However, correlation with the Raman peak is observed: the PL intensity is high where the Raman intensity of A_{1g} is low and vice versa (Fig. 6f), a behavior which is not fully understood. Based on previous PL work on MoS_2 ,^{4,41} it is tempting to associate the low Raman/high PL behavior with the presence of single layer MoSe_2 areas and the high Raman/low PL one with bi-layer MoSe_2 in other areas on the same wafer. This has to be treated with caution though given that an abnormally high PL at room temperature has been reported³⁷ in few-layer MoSe_2 . Finally it is worth noting that uncapped single and bi-layer MoSe_2 have been examined by Raman and PL over a period of time and they have been found to be very stable over at least two weeks while exposed to air (see also ESI†, Fig. S6).

Critical assessment of microstructure and uniformity

The characterization of large area MoSe_2 films is very challenging because most of the techniques which are sensitive to microstructure such as HRTEM are sampling techniques probing only a limited area of the order of (80-100) nm in length. In such length scale, the single crystal quality and thickness uniformity is unambiguously confirmed (Fig. 3) in several sampled areas on the wafer. Low magnification TEM can provide information about thickness uniformity in the few hundred nm scale as for example the TEM image in Fig. S7 (ESI†) which shows a very good thickness uniformity of MoSe_2 over a region that exceeds 250 nm in length. Other techniques, such as STM or SEM probe larger areas in the few tens of a micron- or mm- scale and by using these techniques ((see also ESI†, Figs. S2 and S3) we conclude that the films are continuous with full coverage over the entire 2 inch diagonal substrates and that there are no major thickness variations across the wafer. However these techniques are less sensitive to thickness variations at the level of a single atomic layer and to the existence of microstructure such as grains.

Oriental grain boundaries (GB) retain a crystalline structure and may be of high or low angle. In this case, the pertinent high angle GBs are the orientation twins that have not been identified in our films by RHEED as already discussed above in connection to Fig. 1. The cross sectional HRTEM observations are also consistent, i.e. no twin boundaries were observed.

Regarding low-angle GBs, plan view TEM observations are required. The preparation of such TEM specimens is difficult due to the AlN substrate which renders useless the currently available approaches. Although it was not possible to account for such GBs from plan view TEM, we argue that, if they are present to any significant extent, such GBs would consist of dislocations parallel to the growth direction. In our cross section observations we did not observe any appreciable density of such defects.

The characterization and uniformity assessment of ultrathin (a few ML) MoSe_2 films remain big challenges. In fact, most of the techniques, including XRD, are not sensitive when applied to atomic scale materials. Raman is a technique which has sufficient sensitivity for single layer crystals and is extensively used for graphene and 2D MX_2 -type semiconductors. This provides a rough estimate about thickness and physical properties with micron resolution probing uniformity over a (10-100) μm scale at least. The MoSe_2 films mapped by Raman

over such a range were found to have excellent uniformity, while the same tests repeated in several parts of the wafer yield similar excellent uniformity results.

In summary, despite the difficulties in the characterization of ultrathin films on a large area of the substrate, our investigation using a variety of techniques provide evidence that the films are continuous, covering the entire substrate and that they do not have gross non-uniformities with respect to the thickness and the surface roughness. Moreover, electron diffraction (RHEED) and HRTEM show no evidence for randomly oriented grains or for high (twin) or low angle orientational grains suggesting highly oriented single crystal films epitaxially grown on cm-scale AlN substrates.

Conclusions

In summary, we demonstrate the molecular beam epitaxial growth of large area, highly oriented single crystals of controllable single to few- layer MoSe_2 films on AlN(0001)/Si substrates. We show by HRTEM that MoSe_2 films on AlN(0001) have high structural quality and surface and interface morphology confirmed also by XPS data showing stoichiometric MoSe_2 with no reaction at the interface with AlN. In addition, very good uniformity and excellent stability in air is evidenced by room temperature Raman and photoluminescence. We also show that MoSe_2 can grow with very good quality on Bi_2Se_3 buffer layers and that epitaxial $\text{Bi}_2\text{Se}_3/\text{MoSe}_2$ multilayers can be produced. As a final remark, it is emphasized here the important role of the substrate. Since AlN is a wide band gap material, it offers the benefits of MoSe_2 semiconductor-on-insulator integration scheme creating the prospect for low leakage through the substrate and improved electrostatic control. This is further supported by XPS analysis which indicates sufficiently high CBO and VBO acting as barriers for charge transport through the substrate. Moreover, AlN/Si(111) large area (200 mm and 300 mm) wafers are readily available as they have been developed for several years in the context of III-nitride power and lighting devices. Once high quality epitaxial MoSe_2 is prepared on 300 mm AlN/Si wafers, devices and circuits can be realized on the same wafers, or the MoSe_2 layer can be transferred onto other optimal large area substrates of choice, including flexible or transparent substrates for further device processing. Therefore AlN/Si creates the prospect for low cost wafer-scale manufacturing of MoSe_2 -based devices and circuits when TMD technology becomes mature enough for volume production.

Acknowledgements

The work is supported by the ERC Advanced Grant SMARTGATE-291260- and the National program of excellence (ARISTEIA-745) through the project TOP-ELECTRONICS.

Notes and references

^a Institute of Nanoscience and Nanotechnology, NCSR DEMOKRITOS, GR-15310, Athens, Greece. *E-mail: dimoulas@ims.demokritos.gr.

^b Physics Department, Aristotle University of Thessaloniki, GR-54124 Thessaloniki, Greece.

^c Imec, Kapeldreef 75, Leuven, Belgium.

† Electronic Supplementary Information (ESI) available: Crystal structure of MoSe_2 . Large area STM images of 3 ML MoSe_2/AlN . Large

area optical and SEM images of MoSe₂ films on AlN. GPA lattice strain analysis map of 3ML MoSe₂ deposited on AlN. Band diagrams reconstruction of MoSe₂/AlN and MoSe₂/Bi₂Se₃/AlN. Short scale uniformity investigation of 1ML MoSe₂ on AlN(0001). Stability investigation of 1ML MoSe₂ on AlN(0001). Large area TEM image of MoSe₂ on AlN(0001). See DOI: 10.1039/b000000x/

- 1 Q. H. Wang, K. Kalantar-Zadeh, A. Kis, J. N. Coleman and M. S. Strano, *Nat. Nanotechnol.*, 2012, **7**, 699-711.
- 2 M. Xu, T. Lian, M. Shi and H. Chen, *Chem. Rev.*, 2013, **113**, 3766–3798.
- 3 A. K. Geim and I. V. Grigorieva, *Nature*, 2013, **499**, 419-425.
- 4 K. F. Mak, C. Lee, J. Hone, J. Shan, and T. F. Heinz, *Phys. Rev. Lett.*, 2010, **105**, 136805.
- 5 H. S. Lee, S. W. Min, Y. G. Chang, M. K. Park, T. Nam, H. Kim, J. H. Kim, S. Ryu and S. Im, *Nano Lett.*, 2012, **12**, 446–701.
- 6 H. Fang, C. Battaglia, C. Carraro, S. Nemsak, B. Ozdol, J. S. Kang, H. A. Bechtel, S. B. Desai, F. Kronast, A. A. Unal, G. Conti, C. Conlon, G. K. Palsson, M. C. Martin, A. M. Minor, C. S. Fadley, E. Yablonovich, R. Maboudian and A. Javey, *PNAS*, 2014, **111**, 6198-6202.
- 7 J. S. Ross, P. Klement, A. M. Jones, N. J. Ghimire, Y. Yan, D. G. Mandrus, T. Taniguchi, K. Watanabe, K. Kitamura, W. Yao, D. H. Cobden, and X. Xu, *Nat. Nanotechnol.*, 2014, **9**, 268-272.
- 8 A. Pospischil, M. M. Furchi and T. Mueller, *Nat. Nanotechnol.*, 2014, **9**, 257-261.
- 9 B. Radisavljevic, A. Radenovic, J. Brivio, V. Giacometti and A. Kis, *Nature Nanotech.*, 2011, **6**, 147–150.
- 10 H. Liu, A. T. Neal and P. D. Ye, *ACS Nano*, 2012, **6**, 8563-8569.
- 11 H. Liu and P. D. Ye, *IEEE Electron Device Lett.*, 2012, **33**, (4) 546-548.
- 12 B. Radisavljevic, M. B. Whitwick and A. Kis, *ACS Nano*, 2011, **5**, 9934–9938.
- 13 H. Wang, L. Yu, Y. H. Lee, Y. Shi, A. Hsu, M. L. Chin, L. J. Li, M. Dubey, J. Kong and T. Palacios, *Nano Lett.*, 2012, **12**, 4674-4680.
- 14 Y-H Lee, X. Q. Zhang, W. Zhang, M. T. Chang, C. T. Lin, K. D. Chang, Y. C. Yu, J. T. W. Wang, C. S. Chang, L. J. Li and T. W. Lin, *Adv. Mater.*, 2012, **24**, 2320–2325.
- 15 X. Lu, J. Lin, M. I. B. Utama, X. Gong, J. Zhang, Y. Zhao, S. T. Pantelides, J. Wang, Z. Dong, Z. Liu, W. Zhou and Q. Xiong, *Nano Lett.*, 2014, **14**, 2419–2425.
- 16 X. Wang, Y. Gong, G. Shi, W. L. Chow, K. Keyshar, G. Ye, R. Vajtai, J. Lou, Z. Liu, E. Ringe, B. K. Tay and P. M. Ajayan, *ACS Nano*, 2014, **8**, 5125–5131.
- 17 J. C. Shaw, H. Zhou, Y. Chen, N. O. Weiss, Y. Liu, Y. Huang and X. Duan, *Nano Research*, 2014, **7**, 1-7.
- 18 F. S. Ohuchi, B. A. Parkinson, K. Ueno and A. Koma, *J. Appl. Phys.*, 1990, **68**, 2168-2175.
- 19 Y. Zhang, T. R. Chang, B. Zhou, Y. T. Cui, H. Yan, Z. Liu, F. Schmitt, J. Lee, R. Moore, Y. Chen, H. Lin, H. T. Jeng, S. K. Mo, Z. Hussain, A. Bansil and Z. X. Shen, *Nat. Nanotechnol.*, 2014, **9**, 111-115.
- 20 P. Tsipas, E. Xenogiannopoulou, S. Kassavetis, D. Tsoutsou, E. Golias, C. Bazioti, G. P. Dimitrakopoulos, P. Komninou, H. Liang, M. Caymax and A. Dimoulas, *ACS Nano*, 2014, **8**, 6614-6619.
- 21 P. A. Stadelmann, *Ultramicroscopy*, 1987, **21**, 131-145.
- 22 R. Coehoorn, C. Haas, J. Dijkstra, C. J. F. Flipse, R. A. de Groot and A. Wold, *Phys. Rev. B*, 1987, **35**, 6195-6202.
- 23 S. K. Mahatha, K. D. Patel, K. S. R. Menon, *J. Phys.: Condens. Matter*, 2012, **24**, 475504.
- 24 K. Momma and F. Izumi, *J. Appl. Crystallogr.*, 2011, **44**, 1272-1276.
- 25 D. Gerthsen, E. Hahn, B. Neubauer, V. Potin, A. Rosenauer and M. Schowalter, *Phys. Stat. Sol. (C)*, 2003, **0** (6), 1668-1683.
- 26 M. J. Hytch, F. Houdellier, F. Hüe and E. Snoeck, *Nature*, 2008, **453**, 1086-1089.
- 27 A. Bezinge, K. Yvon, J. Muller, W. Lengaeur and P. Ettmayer, *Solid State Commun.*, 1987, **63**, 141.
- 28 E. Kraut, R. Grant, J. Waldrop and S. Kowalczyk, *Phys. Rev. Lett.*, 1980, **44**, 1620.
- 29 C. I. Wu, A. Kahn, E. S. Hellman and D. N. E. Buchanan, *Appl. Phys. Lett.*, 1998, **73**, 1346-1348.
- 30 C. Gong, H. Zhang, W. Wang, L. Colombo, R. M. Wallace and K. Cho, *Appl. Phys. Lett.*, 2013, **103**, 053513.
- 31 J. Suh, D. Fu, X. Liu, J. K. Furdyna, K. M. Yu, W. Walukiewicz, and J. Wu, *Phys. Rev. B*, 2014, **89**, 115307.
- 32 T. Böker, R. Severin, A. Müller, C. Janowitz, R. Manzke, D. Voss, P. Krüger, A. Mazur and J. Pollman, *Phys. Rev. B*, 2001, **64**, 235305.
- 33 W. S. Yun, S. W. Han, S. C. Hong, I. G. Kim and J. D. Lee, *Phys. Rev. B*, 2012, **85**, 033305.
- 34 S. Horzum, H. Sahin, S. Cahangirov, P. Cudazzo, A. Rubio, T. Serin and F. M. Peeters, *Phys. Rev. B*, 2013, **87**, 125415.
- 35 P. Tonndorf, R. Schmidt, P. Böttger, X. Zhang, J. Börner, A. Liebig, M. Albrecht, C. Kloc, O. Gordan, D. R. T. Zahn, S. Michaelis de Vasconcellos and R. Bratschitsch, *Opt. Express*, 2013, **21**, 4908.
- 36 T. A. Harriman, D. A. Lucca, J. K. Lee, M. J. Klopstein, K. Herrmann and M. Nastasi, *Nuclear Instruments and Methods in Physics Research B*, 2009, **267**, 1232–1234.
- 37 S. Tongay, J. Zhou, C. Ataca, K. Lo, T. S. Matthews, J. Li, J. C. Grossman and J. Wu, *Nano Lett.*, 2012, **12**, 5576–5580.
- 38 J. Mann, Q. Ma, P. M. Odenthal, M. Isarraraz, D. Le, E. Preciado, D. Barroso, K. Yamaguchi, G. von Son Palacio, A. Nguyen, T. Tran, M. Wurch, A. Nguyen, V. Klee, S. Bobek, D. Sun, T. F. Heinz, T. S. Rahman, R. Kawakami and L. Bartels, *Adv. Mater.*, 2014, **26**, 1399-1404.
- 39 N. Kumar, Q. Cui, F. Ceballos, D. He, Y. Wang and H. Zhao, *Nanoscale*, 2014, **6**, 4915-4919.
- 40 Z. Y. Zhu, Y. C. Cheng and U. Schwingenschlögl, *Phys. Rev. B*, 2011, **84**, 153402.
- 41 A. Splendiani, L. Sun, Y. Zhang, T. Li, J. Kim, C. Y. Chim, G. Galli and F. Wang, *Nano Lett.*, 2010, **10**, 1271-1275.